

Article

Effect of Different Iron Phases of Fe/SiO₂ Catalyst in CO₂ Hydrogenation under Mild Conditions

Paphatsara Sirikulbodee^{1,2}, Monrudee Phongaksorn^{1,2}, Thana Sornchamni³, Tanakorn Ratana^{1,2} and Sabaithip Tungkamani^{1,2,*}

¹ Department of Industrial Chemistry, Faculty of Applied Science, King Mongkut's University of Technology North Bangkok, Bangkok 10800, Thailand; sirikulbodee.p@gmail.com (P.S.); monrudee.p@sci.kmutnb.ac.th (M.P.); tanakorn.r@sci.kmutnb.ac.th (T.R.)

² Research and Development Center for Chemical Engineering Unit Operation and Catalyst Design (RCC), King Mongkut's University of Technology North Bangkok, Bangkok 10800, Thailand

³ PTT Innovation Institute, PTT Public Company Limited, Wang Noi, Phra Nakhon Si Ayutthaya 13170, Thailand; thana.s@pttplc.com

* Correspondence: sabaithip.t@sci.kmutnb.ac.th; Tel.: +66-8120-89383

Abstract: The effect of different active phases of Fe/SiO₂ catalyst on the physio-chemical properties and the catalytic performance in CO₂ hydrogenation under mild conditions (at 220 °C under an ambient pressure) was comprehensively studied in this work. The Fe/SiO₂ catalyst was prepared by an incipient wetness impregnation method. Hematite (Fe₂O₃) in the calcined Fe/SiO₂ catalyst was activated by hydrogen, carbon monoxide, and hydrogen followed by carbon monoxide, to form a metallic iron (Fe/SiO₂-h), an iron carbide (Fe/SiO₂-c), and a combination of a metallic iron and an iron carbide (Fe/SiO₂-hc), respectively. All activated catalysts were characterized by XRD, Raman spectroscopy, N₂ adsorption–desorption, H₂-TPR, CO-TPR, H₂-TPD, CO₂-TPD, CO-TPD, NH₃-TPD, and tested in a CO₂ hydrogenation reaction. The different phases of the Fe/SiO₂ catalyst are formed by different activation procedures and different reducing agents (H₂ and CO). Among three different activated catalysts, the Fe/SiO₂-c provides the highest CO₂ hydrogenation performance in terms of maximum CO₂ conversion, as well as the greatest selectivity toward long-chain hydrocarbon products, with the highest chain growth probability of 0.7. This is owing to a better CO₂ and CO adsorption ability and a greater acidity on the carbide form of the Fe/SiO₂-c surface, which are essential properties of catalysts for polymerization in FTs.

Keywords: CO₂ hydrogenation; iron carbides; carbonization; low temperature; low pressure



Citation: Sirikulbodee, P.; Phongaksorn, M.; Sornchamni, T.; Ratana, T.; Tungkamani, S. Effect of Different Iron Phases of Fe/SiO₂ Catalyst in CO₂ Hydrogenation under Mild Conditions. *Catalysts* **2022**, *12*, 698. <https://doi.org/10.3390/catal12070698>

Academic Editors: Ghulam Yasin, Shumaila Ibraheem and Tuan Anh Nguyen

Received: 17 May 2022

Accepted: 23 June 2022

Published: 25 June 2022

Publisher's Note: MDPI stays neutral with regard to jurisdictional claims in published maps and institutional affiliations.



Copyright: © 2022 by the authors. Licensee MDPI, Basel, Switzerland. This article is an open access article distributed under the terms and conditions of the Creative Commons Attribution (CC BY) license (<https://creativecommons.org/licenses/by/4.0/>).

1. Introduction

Carbon dioxide (CO₂) is the most abundant greenhouse gas accumulated in the atmosphere and a major contributor to climate change. Reducing CO₂ emissions, CO₂ capture, and utilization have been considered as key technologies to solve these environmental problems [1]. Among all the proposed approaches, conversion of CO₂ into chemicals and renewable fuels has gained the great interest because of environmental and economic benefits. CO₂ is an attractive renewable source of carbon for the production of value-added chemicals, such as methanol, formic acid, and hydrocarbon compounds, through many reactions [2–5]. Although CO₂ is a thermodynamically stable and kinetically inert molecule due to a double covalent bond between carbon and two oxygen atoms, the reaction of CO₂ with explosive H₂ and CH₄ gas can be achieved under severe conditions [4]. Dry methane reformation using CO₂ mainly produces syngas (CO and H₂), which is important feedstock for various chemical industries. Many works also revealed the success of producing synthetic hydrocarbon fuels through a CO₂ hydrogenation reaction using Fischer–Tropsch synthesis (FTs) [6]. It is well known that the conventional synthesis of long-chain hydrocarbons commonly produces hydrocarbons from syngas (a mixture of

H₂:CO) [7,8]. The modification of synthesis using CO₂ as a feedstock proceeds via two reactions. The conversion of CO₂ to CO via the reverse water-gas shift (RWGS) reaction (Equation (1)) is the initial reaction, followed by hydrogenation to produce long-chain hydrocarbons. (Equation (2)) [9,10].



Among group VIII B metals, cobalt (Co) and iron (Fe) are commonly used as commercial active metals for CO hydrogenation via FTs [11]. However, the active forms of Co and Fe are different. Previous studies accepted that metallic cobalt is the main active form of Co-based catalyst, while carbide is the main active form of Fe based catalyst [12]. Conventional FT catalysts are usually designed to exhibit high catalytic selectivity to C₅₊ hydrocarbons and low selectivity toward C₁–C₄ hydrocarbon products [13,14]. Under typical FTs conditions using H₂ and CO₂, Co is selective to produce methane and small amounts of lower hydrocarbons (C₂–C₄) [15]. The difference in selectivity of CO₂ hydrogenation over Co and Fe catalyst is owing to the difference in RWGS activity of both catalysts [16]. Fe catalysts could function efficiently for RWGS assumed to be a reaction step in the primary pathway for CO₂ hydrogenation via FTs [17], whereas Co catalyst exhibits lower activity. It has been confirmed that Fe is the most favorable characteristic for hydrogenation of CO₂ to produce long-chain hydrocarbons. Therefore, most studies on CO₂ hydrogenation via FTs have focused on using iron-based catalysts [18–20].

Typically, fresh calcined Fe catalyst mainly consists of hematite (Fe₂O₃), which is considered an inactive phase for CO₂ hydrogenation [21]. This phase must be activated under appropriate conditions into an active form for the reaction. Normally, H₂, CO and syngas are used as reducing agents for the reduction of Fe catalyst [21]. The change of Fe phases can occur during the reduction, as well as CO₂ hydrogenation [22]. As mentioned previously, iron carbide is the main active form of Fe catalyst in FTs [23]. The phase compositions of the active sites for Fe catalyst in FTs have been intensively studied and reported as a key control of the reaction mechanism [24]. Moreover, a large amount of research concerning the activation effects on Fe catalysts has been devoted to unraveling the relationships between catalyst textural properties, phase transformations, and CO₂ hydrogenation performances [25–27]. The phases of active sites could be the iron oxide, metal and carbide after activation, and self-formation under reaction conditions. Iron oxide as magnetite (Fe₃O₄) is always found to be present in the catalyst under typical FTs conditions [28]. The unsupported iron catalyst was initially reduced to metallic iron (α-Fe) under H₂ activation. After reaction, the spent Fe catalyst presents partially oxidized forms of Fe²⁺ and Fe³⁺ mixed with metallic and carbide forms. The mixture of these iron species, except Fe₃C, were believed to be the main active site for the hydrogenation of CO₂ to CO. Liu et al. [26] prepared an iron carbide as the Fe₅C₂ phase by carbonization of ferrous oxalate precursors under CO flow, and investigated the catalytic performance of Fe₅C₂ and K-modified Fe₅C₂ in CO₂ hydrogenation. It was found that Fe₅C₂ is an active site for RWGS and chain growth in FTs reactions. An increase in the basicity of alkali metal-added catalyst was found to improve CO₂ adsorption, promote long-chain hydrocarbon selectivity through only CO-intermediate routes, and inhibit the adsorption of H species [29]. Consequently, the adsorption behavior of CO₂, H₂, and CO-intermediate on iron species significantly affects the catalytic performance.

Although certain works have reported the relation of iron phases to the catalyst surface and the CO hydrogenation performance under various ranges of reaction conditions [30,31], the effect of the iron phases on CO₂ hydrogenation is still ill-understood due to the more complicated mechanism [32]. Accordingly, the study of different iron phases derived from the different activation procedures on the product selectivity of CO₂ hydrogenation is of interest, and it should be evaluated with the adsorption behavior of reactants and an

intermediate on these active sites. To maintain the active site as the phase obtained after the pretreatment, the CO₂ hydrogenation should be performed under mild conditions.

In this work, the iron oxide on the calcined catalyst was activated to form a metallic iron, an iron carbide, and a combination of a metallic iron and an iron carbide. To achieve all those forms, the relevant condition of the activation by H₂ reduction and/or carbonization was necessary. The Fe/SiO₂ catalyst was prepared by an incipient wetness impregnation method. Then, the calcined catalyst was activated using two different procedures: the pre-reduction of the catalyst in hydrogen followed by the carbonization of the catalyst in carbon monoxide. For the comparison, the one-step reduction of the catalyst in hydrogen was also performed. The reducibility behavior of different iron phases formed during the activation with different reducing agents was studied by H₂-TPR and CO-TPR. Moreover, the effect of different iron phases on the textural, structural, and adsorption properties of the Fe/SiO₂ catalyst was investigated by means of N₂ adsorption–desorption analysis, X-ray diffraction (XRD), Raman spectroscopy, and temperature-programmed desorption (TPD). Then, catalytic performance in CO₂ hydrogenation over the different iron phases was performed at 220 °C under atmospheric pressure. Herein, the relation of physio-chemical properties and catalytic performance on different iron phases obtained by different activated procedures was verified.

2. Results and Discussion

2.1. Reduction of Iron Oxide

As mentioned in the introduction, this work aims to evaluate the CO₂ hydrogenation performance over the silica-supported iron catalyst when the iron oxide on the calcined catalyst was activated by different procedures to form a metallic iron (Fe/SiO₂-h), an iron carbide (Fe/SiO₂-c), and a combination of a metallic iron and an iron carbide (Fe/SiO₂-hc). To achieve all these forms, the relevant conditions of the activation (the reduction or the carbonization) were necessary. Thus, TPR analysis of silica-supported iron catalyst using the different reducing gases (H₂ and CO), as well as the reduction steps, was employed to determine the proper conditions of the catalyst reduction and/or the carbonization. The TPR results are presented in Figure 1. The H₂-TPR profile of calcined Fe/SiO₂ catalyst in the temperature range between 50 °C and 800 °C (Figure 1a) represents four reduction peaks of iron oxide species to the iron metal phase on the calcined silica-supported iron catalyst. The first peak around 200–370 °C can be assigned to the transformation of hematite (Fe₂O₃) to magnetite (Fe₃O₄). The second peak centered at 420 °C is attributed to the reduction of Fe₃O₄ to Wüstite (FeO), and the third peak centered at about 500 °C is due to the reduction of remaining Fe₃O₄ or hardly reducible Fe oxide species [27]. The difficulty of Fe₃O₄ reduction was monitored because magnetite contains both Fe²⁺ and Fe³⁺ (formulated as FeO·Fe₂O₃) [33]. The highest temperature peak centered at 600 °C can be ascribed to the reduction of FeO to metallic Fe (α -Fe) [34]. Although the H₂-TPR results suggest that the reduction curve ends at 650 °C, the reduction temperature has been chosen at temperature (500 °C), which is slightly lower than the calcined temperature (550 °C), to avoid the sintering problem. To activate iron oxide species to a metallic iron, the in situ isothermal reduction of the calcined Fe/SiO₂ catalyst has been selected at 500 °C for 16 h in the flow of pure H₂ (H₂-reduced Fe/SiO₂ catalyst, coded as Fe/SiO₂-h).

To study the carbonization of the silica-supported iron catalyst, the CO-TPR measurement of the calcined Fe/SiO₂ catalyst (Figure 1b) was investigated. At the beginning temperature (50–200 °C), the CO-TPR profile shows a slight drift of baseline, probably due to pre-adsorbed CO on the surface of the catalyst at low temperature. The CO-TPR profiles of iron oxide on the calcined Fe/SiO₂ catalyst (Figure 1b) show three regions of peak appearance. For the first region between 200 °C to 400 °C, the peak centered at 250 °C is ascribed to the formation of Fe₃O₄ from the carbonization of Fe₂O₃ (Equation (3)). The reduction of Fe₃O₄ by CO can transform to FeO (Equation (4)) and iron carbide (Fe₅C₂, Equation (5)) [35]. As a result, the shoulder reduction peak at 300 °C, finishing at about 400 °C, is associated with the reduction of Fe₃O₄ to FeO and/or Fe₅C₂. A broad peak in the

second region between 400 °C and 600 °C relates to the reduction of iron carbide and a part of the iron oxide species to α -Fe (Equation (6)), since the Fe_5C_2 can be transformed to α -Fe. Peaks at temperatures higher than 600 °C correlate to the deposited carbon on α -Fe from the Boudouard reaction (Equation (7)) [36–39]. Our results are in good agreement with Tahari et al. [39], who has suggested a three-step sequential process for the carbonization of the Fe/SiO₂ catalyst ($\text{Fe}_2\text{O}_3 \rightarrow \text{Fe}_3\text{O}_4 \rightarrow \text{FeO} \rightarrow \alpha$ -Fe). Then, the change in the reduction of the calcined Fe/SiO₂ catalyst with CO for this work is considered to trend as following: $\text{Fe}_2\text{O}_3 \rightarrow \text{Fe}_3\text{O}_4$, iron carbides and/or FeO $\rightarrow \alpha$ -Fe [37–39]. Consequently, the condition for the carbonization of the calcined Fe/SiO₂ catalyst to form iron carbide has been drowning at 400 °C for 2 h in 10% CO balanced with He (CO-carbonized Fe/SiO₂ catalyst, coded as Fe/SiO₂-c).

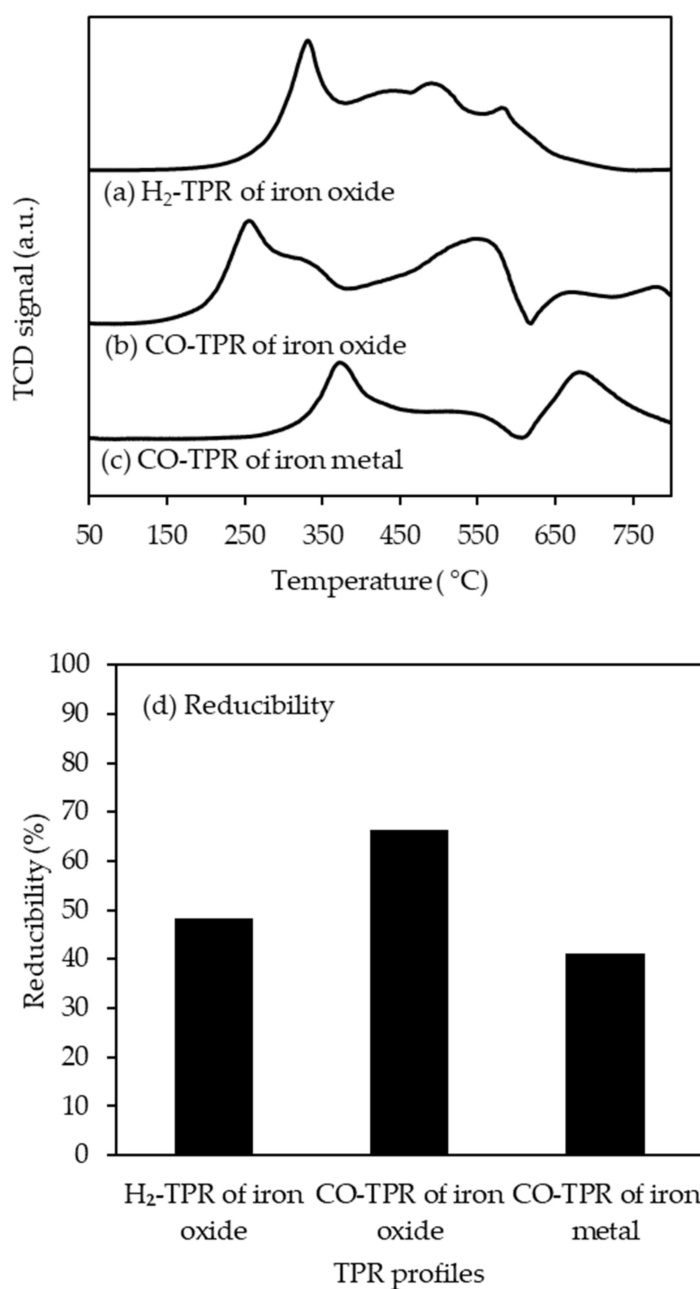
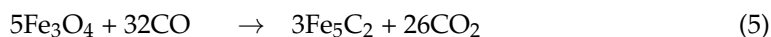
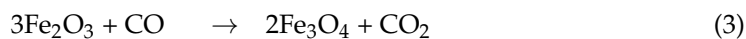


Figure 1. (a) H₂-TPR profile of calcined Fe/SiO₂ catalyst, (b) CO-TPR profile of calcined Fe/SiO₂ catalyst, (c) CO-TPR profile of reduced Fe/SiO₂ catalyst, and (d) reducibility of the different TPR profiles of Fe/SiO₂ catalyst.



A combination form between a metallic iron and an iron carbide was designed to be prepared by the carbonization with CO after the reduction of the calcined iron catalyst with H₂. Therefore, the carbonization of the Fe/SiO₂-h was analyzed using the CO-TPR measurement, and the CO-TPR profile of the Fe/SiO₂-h is illustrated in Figure 1c. Three peaks of the CO-TPR profile of Fe/SiO₂-h were detected as a sharp peak at 375 °C, a shoulder peak from 450 °C to 600 °C, and a peak at a temperature higher than 600 °C, corresponding to the transformation of the iron metal to the iron carbide, the iron carbide to the metallic iron, and the carbon deposition on the catalyst surface, respectively [40]. It must be noticed that a similar profile was observed on the CO-TPR profile of the calcined catalyst (Figure 1b), but the first peak in Figure 1b disappears. A shoulder peak in Figure 1b seems to be the first peak of CO-TPR of iron metal (Figure 1c), which shifts to a higher temperature. This peak is due to the carbonization of metallic iron being more difficult compared to iron oxide. Accordingly, the two-step activation using the reduction with pure H₂ at 500 °C for 16 h, followed by the carbonization with 10% CO/He at 400 °C for 2 h, form a combined iron carbide and metallic iron of the calcined Fe/SiO₂ catalyst (H₂-reduced and CO-carbonized Fe/SiO₂ catalyst, coded as Fe/SiO₂-hc).

The reducibility of each TPR measurement is summarized in Figure 1d. The reducibility was calculated based on the peak area of TPR profiles, which is the amount of reducing agent (H₂ or CO) consumed for the reduction in the range of temperature lower than 600 °C, which only involves the change of iron phase in the catalyst. As seen in Figure 1d, the reducibility of the calcined Fe/SiO₂ catalyst in H₂-TPR is 48.36%, while the greatest reducibility (66.38%) was obtained for the CO-TPR of the calcined Fe/SiO₂ catalyst. This indicates that the calcined Fe/SiO₂ catalyst can be more activated by CO compared to H₂. However, the CO-TPR of the reduced Fe/SiO₂ catalyst (Fe/SiO₂-h) presents a reducibility of 41.09%. This could be explained by the calcined Fe/SiO₂ catalyst being initially reduced by hydrogen during the pretreatment step, thus the least reducibility in the second step was observed when CO-TPR performed.

2.2. Textural and Structural Characteristics of Materials

After obtaining suitable activation conditions from TPR measurements, three activation conditions were applied for the activation of the calcined Fe/SiO₂ catalyst. The one-step H₂ reduction and the one-step CO carbonization of the calcined Fe/SiO₂ catalyst were performed to produce the metallic iron (Fe/SiO₂-h) and iron carbide (Fe/SiO₂-c), respectively. The two-step H₂ reduction followed by CO carbonization of the calcined Fe/SiO₂ catalyst was employed to gain the mixture of metallic iron and iron carbide (Fe/SiO₂-hc) on the catalyst surface. The iron phase of the calcined Fe/SiO₂ catalyst and all activated catalysts (Fe/SiO₂-h, Fe/SiO₂-c, and Fe/SiO₂-hc) were investigated using XRD (Figure 2a), and the carbonaceous surface was confirmed using Raman spectroscopy (Figure 2b,c). The textural properties of all samples were characterized by N₂ adsorption-desorption isotherm, expressed in Table 1.

According to the literature [41–43], the activation of catalysts by carbonization with CO under a temperature range of 230–450 °C can produce Fe carbide with mixed phases. Therefore, catalysts activated by this process were assumed to have Fe carbide, and the appearance of Fe carbide was confirmed by XRD and Raman spectroscopy techniques, although the XRD result presents a poor signal for the diffraction peaks of Fe/SiO₂-hc observed at 42.9°, 43.6°, 44.6°, 49.3°, and 65.0°. This reflects the overlapping of the Fe

carbide and Fe metallic phase. The XRD pattern of the Fe/SiO₂-h catalyst presents peaks at 2θ of 44.6° and 65.0° which correspond to the Fe metallic phase. A broader peak at 2θ of 44.6° observed for the Fe/SiO₂-hc catalyst, compared to Fe/SiO₂-h which presents a sharp peak, could indicate mixed phases (i.e., metallic phase and carbide phase) occurring in Fe/SiO₂-hc catalyst. The change of peak shape from a sharp peak presenting the Fe metallic phase to a broader peak implies a decrease in the crystalline structure of the Fe metallic phase, which is partially transformed to the Fe carbide phase.

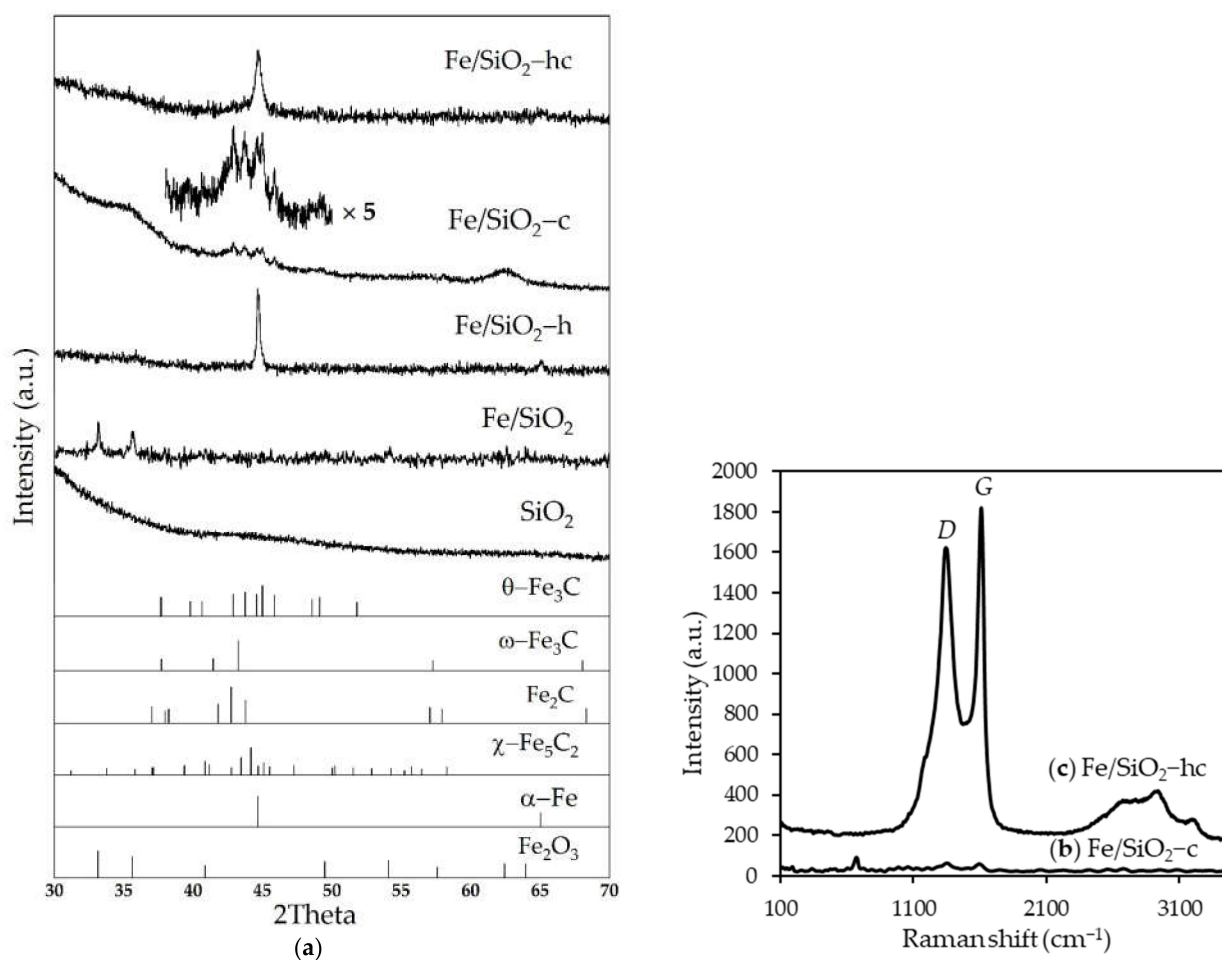


Figure 2. (a) XRD profiles of the calcined Fe/SiO₂ catalyst and all activated Fe/SiO₂ catalysts, and Raman spectra of (b) Fe/SiO₂-c and (c) Fe/SiO₂-hc catalysts.

Table 1. Textural and structural characteristics of catalysts.

Samples	N ₂ Adsorption-Desorption				XRD
	S _{BET} (m ² ·g ⁻¹)	V _{μp} (cm ³ ·g ⁻¹)	V _{tp} (cm ³ ·g ⁻¹)	D _p (nm)	Crystallite Size (nm)
SiO ₂	543	0.50	0.59	3.61	-
Fe/SiO ₂	427	0.30	0.34	3.17	35.6 ^a
Fe/SiO ₂ -h	213	0.18	0.21	3.94	33.2 ^b
Fe/SiO ₂ -c	345	0.27	0.29	3.37	n.a. ^c
Fe/SiO ₂ -hc	224	0.19	0.21	3.83	18.7 ^b

^a calculated by XRD of the fresh catalyst with the diffraction line of 2θ at 33.2 for Fe₂O₃ using the Scherrer equation.

^b calculated by XRD of Fe/SiO₂-h and Fe/SiO₂-hc catalysts with the diffraction line of 2θ at 44.6 for Fe^o using the Scherrer equation. ^c n.a. is not available because of the detection limit.

Ding et al. [44] also reported that the carbonization ability of reduced iron phases is ordered as α -Fe > FeO > Fe₃O₄. Hence, metallic iron (α -Fe) is converted more easily into iron carbide species than other oxide phases in carbonization reactions [37]. Moreover, when Fe/SiO₂-h is activated with CO (Fe/SiO₂-hc), the average crystallite size of Fe is decreased from 33.2 nm to 18.7 nm, implying a greater metal dispersion. However, the fingerprint of the carbide form did not obviously appear in this diffractogram. As displayed in Figure 2, a broad diffraction peak of the Fe/SiO₂-c corresponds to the Fe carbide phase. The XRD diffraction pattern of Fe/SiO₂-c is rarely identified when presented with the diffractogram of other samples because of its small crystallite size. The Fe carbide crystal size of the Fe/SiO₂-c was very small due to measurement constraints and therefore could not be accurately calculated. However, the diffractogram of the Fe/SiO₂-c catalyst was remeasured (Figure 2a with 5 times magnification). Three peaks of iron carbide pattern were monitored in this diffractogram, similarly to the work of Jedrzejewska [45]. The diffraction peaks of Fe/SiO₂-c at 2θ of 42.84°, 43.68°, 44.58°, 44.98°, 45.24°, and 45.82° are assigned to the mixed phases of metallic iron and iron carbide (i.e., α -Fe, Fe₂C, θ -Fe₃C, ω -Fe₃C, χ -Fe₅C₂). Therefore, it could be confirmed that the iron carbide was formed during the carbonization process.

The Raman spectra of Fe/SiO₂-hc and Fe/SiO₂-c are depicted in Figure 2b,c. Two broad peaks at around 1340 and 1590 cm⁻¹ are attributed to the D- and G-band of carbon, respectively. Generally, the D-band originates from the presence of defects and disordered carbon, and the G-band can be described as the graphitic carbon [46]. Therefore, this result indicates the presence of amorphous carbon and graphitic carbon on the surface. A metallic phase encapsulated by graphitic carbon may occur on the surface and it could be the source of carbon during CO₂ hydrogenation. Moreover, it is obviously seen that the intensity of the Raman spectra obtained from Fe/SiO₂-hc is significantly greater than that of Fe/SiO₂-c. This could be interpreted as the surface carbon content on Fe/SiO₂-hc being greater than that in Fe/SiO₂-c.

The textural properties of the calcined and all activated Fe/SiO₂ catalysts, including the BET surface area (S_{BET}), micropore volume ($V_{\mu\text{p}}$), total pore volume (V_{tp}) and average pore diameter (D_{p}), are summarized in Table 1. The N₂ adsorption-desorption isotherm, pore volume, and pore size distribution of all tested samples are displayed in Figure 3. The N₂ adsorption-desorption isotherms for all samples are type IV according to the IUPAC classification [47]. The different activation conditions did not change the shape of the N₂ adsorption-desorption isotherms, which mainly results from the support material. However, the desorption curve and the adsorption curve cannot coincide with each other, indicating the presence of a hysteresis loop. The p/p_0 for the hysteresis loop of all samples is approximately 0.4–0.7, demonstrating the existence of mesoporous structure. According to the appearance of this structure, the pore size distribution can be verified by the BJH method. Moreover, the results from the t -plot and MP method present the existence of micropore structure. By analyzing the textural properties of all samples in Table 1, a decrease of S_{BET} , $V_{\mu\text{p}}$, V_{tp} , and D_{p} , in comparison with SiO₂ support, except the average pore diameter of Fe/SiO₂-h, can be observed.

Table 1 discloses the textural and structural characteristics of the catalysts. The results show that the calcined Fe/SiO₂ catalyst has the highest BET surface area (427 m²/g). The BET surface areas of all activated Fe/SiO₂ catalysts were dropped from the SiO₂ support and calcined Fe/SiO₂ catalyst. The average pore distribution (Figure 3) shows a decrease in the peak intensity of micropore distribution of all activated Fe/SiO₂ catalysts. Among the activated catalysts, Fe/SiO₂-h has the lowest BET surface area with the small micropore volume and the largest pore diameter. This is due to the pore-blocking effect of a large metal particle size after pretreatment. This could be supported by the evidence from a decrease in micropore distribution from Figure 3. The comparison between the reduced catalyst (Fe/SiO₂-h) and carbonized catalysts (Fe/SiO₂-hc and Fe/SiO₂-c) presents an increase in surface area of the carbonized catalyst. This could be explained by the carbonization of iron oxide providing a variety of iron species, which is not easily aggregated during

pretreatment [48]. Thus, a small particle size of the iron species was obtained. When comparing the carbonized catalysts, the Fe/SiO₂-c establishes the highest BET surface area with the greatest micropore volume and the smallest pore diameter. It could be ascribed to large iron metal particles formed during the first H₂ reduction of Fe/SiO₂-hc, which were further carbonized, leading to larger particle size of iron species.

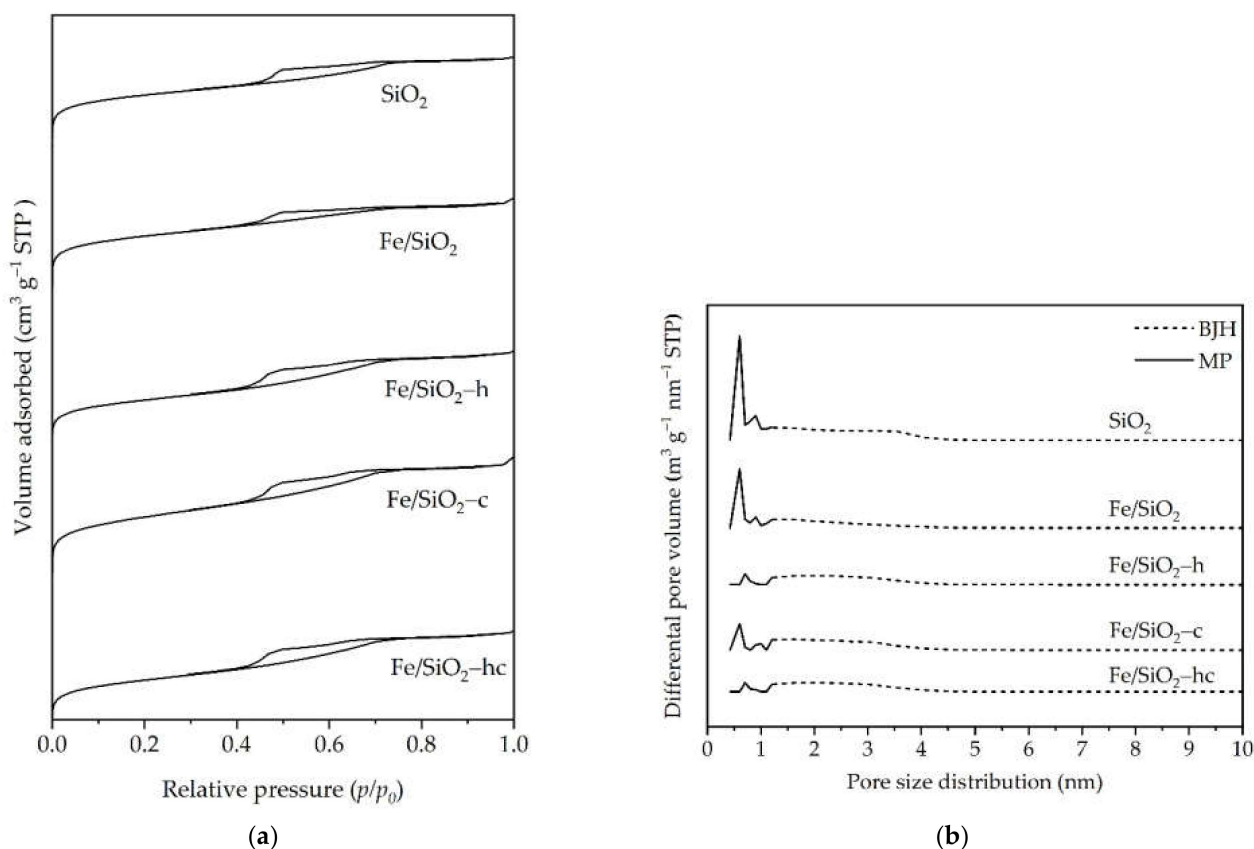


Figure 3. (a) N₂ adsorption–desorption isotherms and (b) pore volume and size distribution of silica support, the calcined Fe/SiO₂ catalyst, and all activated Fe/SiO₂ catalysts.

2.3. Adsorption Behavior of Materials

The activation conditions have a significant impact on the iron phase, resulting in the different textural properties. The XRD data and Raman spectrum have clearly confirmed the formation of the metallic iron phase after the reduction with H₂, and the formation of iron carbide after the carbonization with CO atmosphere. A form of the iron carbide and the metallic iron combination is produced after the two-step activation, the reduction in H₂ and subsequently carbonization in CO. These iron phases have acted as the active site for CO₂ hydrogenation in the catalytic tests. Likewise, the CO₂ hydrogenation performance of the catalysts depends upon the adsorption and desorption abilities of the reactants and intermediates by the different active sites. Moreover, the selectivity of long-chain hydrocarbons also relies on the acidity and basicity of the catalyst surface. Consequently, the effects of iron phases on the adsorption–desorption of the reactants and an intermediate, as well as the surface acidity and basicity, were preliminary appraised and further related to the performance of the catalysts. Therefore, TPD of H₂, CO, CO₂, and NH₃ were carried out to elucidate the adsorption–desorption properties of Fe/SiO₂-h, Fe/SiO₂-c, and Fe/SiO₂-hc.

H₂-TPD was performed to examine the adsorption–desorption of hydrogen on the iron species of H₂-reduced and CO-carbonized catalysts. The results are presented in Figure 4a. It can be seen that H₂-TPD profiles of all catalysts show H₂ thermal desorption in the temperature ranges from 50–800 °C. In low temperature regions (<250 °C), the desorption peak centered around 90 °C was markedly observed only on carbonized catalysts (Fe/SiO₂-

hc and Fe/SiO₂-c). For the reduced catalyst (Fe/SiO₂-h), the profile also illustrates the desorption of H₂ in this temperature region as a low intense broad peak. The desorption in these low temperature regions corresponds to the H species weakly adsorbed on the metallic iron surface. This is confirmed by Bozso and Zhang, [49,50]. They report that the H₂ thermal desorption peaks on Fe single-crystal surfaces, and the H species weakly adsorbed on the metallic iron surface, occurred at around 100 °C.

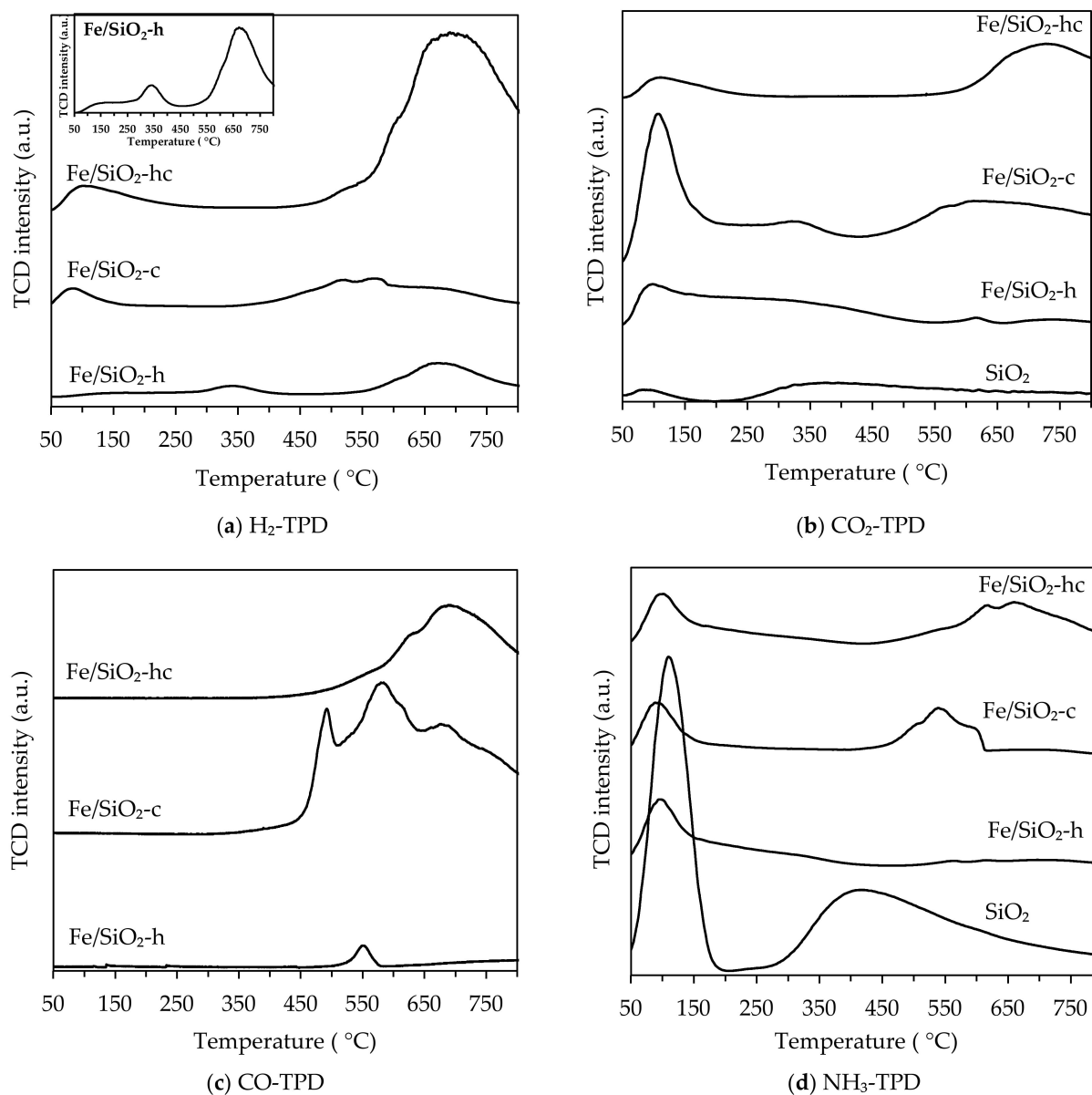


Figure 4. (a) H₂-TPD profiles, (b) CO₂-TPD profiles, (c) CO-TPD profiles, and (d) NH₃-TPD profiles of Fe/SiO₂-h, Fe/SiO₂-c and Fe/SiO₂-hc catalysts.

In the temperature range from 250 °C to 400 °C, the H₂ thermal desorption was only observed on the Fe/SiO₂-h catalyst. The intense peak appearing at 350 °C results from the H species being more strongly adsorbed on metallic iron species. As reported in the literature [51], the H₂ desorption above 300 °C is due to OH species present on the non-reduced oxide surfaces of the catalysts.

In the higher desorption temperature (>400 °C), the H₂ desorption profiles show intense peaks for all catalysts. This could be attributed to the desorption of H species strongly chemisorbed on the surface of the catalyst, which is a combination of the decomposition of

surface CH species and the cleavage of surface OH species [50]. According to the literature [50], the desorption peaks of reduced and carbonized catalysts at higher temperatures are ascribed to the H species adsorbed on the surface carbon of the iron carbide. These species may have existed in the form of CH_x . Noticeably, a large, intense peak recorded at a high temperature was observed for Fe/SiO₂-hc, indicating the decomposition of a large amount of surface CH_x species. This relates to the Raman results, which report the presence of carbon deposition on the surface and the surface CH content on Fe/SiO₂-hc is greater than that in Fe/SiO₂-c.

In this study, the profile of H₂-TPD is also used to examine the iron active species, the calculation of which was based on the peak area of H₂ desorption in low temperature ranges (< 250 °C) because of H adsorbed on metallic iron species. The desorption peak of the carbonized catalysts presents a more intensive signal compared to that of the reduced catalyst. This could indicate that the metallic iron contents are higher on the surfaces of the carbonized catalysts than on the reduced catalyst. This corresponds to the result of BET and XRD. The total amount of hydrogen adsorbed on the surface of the catalysts are in the following order: Fe/SiO₂-h (871.9 μmol/g) < Fe/SiO₂-c (1264.7 μmol/g) < Fe/SiO₂-hc (5699.3 μmol/g) (Table 2). It is envisaged that these H-adsorbed species would exert a significant influence on behavior of the catalysts in hydrogenation of CO₂.

Table 2. The amount of H₂ and CO calculated from H₂-TPD and CO-TPD profiles of all activated Fe/SiO₂ catalysts.

Catalysts	Desorbed Amount of H ₂ (μmol/g)				Desorbed Amount of CO (mmol/g)			
	Weak	Medium	Strong	Total	Weak	Medium	Strong	Total
Fe/SiO ₂ -h	25.6	76.9	769.4	871.9	-	-	1.9	1.9
Fe/SiO ₂ -c	204.9	-	1059.7	1264.7	-	-	98.0	98.0
Fe/SiO ₂ -hc	432.1	-	5267.2	5699.3	-	-	68.6	68.6

The CO₂ adsorption capability of silica support and all activated catalysts (Fe/SiO₂-h, Fe/SiO₂-hc, and Fe/SiO₂-c) were investigated by CO₂-TPD because nonpolar CO₂ molecules are acidic gas, which prefer to adsorb on the basic sites [52]. The CO₂-TPD profiles (Figure 4b) exhibit peaks of CO₂ thermal desorption in the three temperature ranges from 50–800 °C: low, moderate, and high temperature corresponding to the weak, medium, and strong basic site on the surface.

In the low temperature region (50–200 °C), the desorption peak was observed for support and all catalysts, indicating the desorption of CO₂ weakly adsorbed on the catalyst surface. The CO₂-TPD profile of silica support, Fe/SiO₂-h, and Fe/SiO₂-hc displayed similar broad peaks with low intensity centered at around 110 °C due to the low basic site. The distinct peak of the desorption was observed on Fe/SiO₂-c and located at approximately 120 °C. This is attributed to the large amount of CO₂ desorption from weakly adsorbed on the basic site of the carbide catalyst. According to the results of XRD, pore size distribution and H₂-TPD, small particle sizes with high surface area of iron oxide and iron carbide species provide a large amount of basic site. The desorption peaks of CO₂ with low intensity in moderate temperature regions (200–400 °C), referring to medium basic sites, were found in silica support, Fe/SiO₂-h, and Fe/SiO₂-c. The CO₂ desorption profile of silica support and the Fe/SiO₂-h catalyst shows a tailing curve, while a cambered peak at 350 °C was observed for the Fe/SiO₂-c catalyst. However, this type of basic site was not observed in the Fe/SiO₂-hc.

In the high temperature region (> 400 °C), only CO₂-TPD profiles of the carbonized catalysts, Fe/SiO₂-hc and Fe/SiO₂-c, exhibit the broad peak with high intensity, corresponding to desorption of CO₂ strongly adsorbed on basic sites. Comparing the H₂-reduced catalyst (Fe/SiO₂-h) and carbonized catalyst, the basicity of the surface over the carbonized catalyst is higher than that of the reduced catalyst. Among the carbonized catalysts, the Fe/SiO₂-c catalyst presents the highest basicity relating to the high amount of CO₂ desorption. It

could be explained by the iron carbide being more reactive toward electropositive elements [53]. The carbon atom in a carbon dioxide molecule is electrophilic, while the oxygen atom is nucleophilic [54]. Hence, the carbonization significantly promotes the alkalinity of the catalyst surface, enhancing CO₂ adsorption capability [29]. The CO₂ adsorption capability relates to the desorbed amount of CO₂, presented in Table 3. Here, the CO₂ adsorption capability within the investigated temperature range was found to increase in the following sequence: Fe/SiO₂-h (956.4 μmol/g) < SiO₂ (1620.9 μmol/g) < Fe/SiO₂-hc (2783.8 μmol/g) < Fe/SiO₂-c (3312.0 μmol/g). As seen, the iron carbide phase has the highest CO₂ capability, while the iron metal phase has the lowest CO₂ adsorption capability. As compared with Fe/SiO₂-c, the decreasing CO₂ adsorption capability of Fe/SiO₂-hc is a result of the existence of the iron metal phase on the catalyst surface. The desorbed CO₂ amount of the Fe/SiO₂-h is lower than that of SiO₂ due to the blocking effect of the metallic iron particle.

Table 3. The amount of CO₂ and NH₃ calculated from CO₂-TPD and NH₃-TPD profiles of all activated Fe/SiO₂ catalysts.

Catalysts	Desorbed Amount of CO ₂ (μmol/g)				Desorbed Amount of NH ₃ (mmol/g)			
	Weak	Medium	Strong	Total	Weak	Medium	Strong	Total
SiO ₂	147.9	1473.1	-	1620.9	858.5	1128.0	-	1986.5
Fe/SiO ₂ -h	459.3	245.7	251.4	956.4	214.6	-	22.0	236.6
Fe/SiO ₂ -c	1981.6	151.1	1179.3	3312.0	282.1	-	357.1	639.2
Fe/SiO ₂ -hc	467.1	-	2316.7	2783.8	192.2	-	111.1	303.2

For the CO₂ hydrogenation reaction aspect, CO₂ reacts with H₂ to produce CO via RWGS reaction in the first step. The adsorbed CO acting as intermediate species in the reaction may react with adsorbed H and adsorbed OH presented on the catalyst surface, leading to the formation of water and chemisorbed methylene (:CH₂) for the hydrocarbon synthesis [55]. To understand CO₂ hydrogenation performance of the catalysts, the ability of CO adsorption and desorption on the active site of the catalyst is therefore necessary. In this work, this ability was determined using the CO-TPD measurement. The CO desorption peaks in the CO-TPD profiles (Figure 4c) of all activated catalysts begin at about 400 °C, corresponding only to the strong chemisorbed CO. Obviously, the CO₂ desorption peak of the carbonized catalyst is much higher than that of the reduced catalyst, resulting from high CO adsorbed on a high surface area of small particles of metal carbide species mentioned in the previous results. The cause of the appearance of CO desorption peaks at a high temperature range is attributed to CO desorption from recombination of dissociated carbon and oxygen on the catalyst surface [56]. The smallest desorption peak found in the CO-TPD profile of the Fe/SiO₂-h catalyst relates to the adsorbed CO on a small surface area of large particle size of metallic iron species (Fe/SiO₂-h), confirmed by the characterized results. The total amount CO desorption of all activated catalysts is in the sequence: Fe/SiO₂-h (1.9 mmol/g) < Fe/SiO₂-hc (68.6 mmol/g) < Fe/SiO₂-c (98.0 mmol/g). This implies that the CO molecules produced from RWGS reaction are rarely adsorbed on metallic iron sites of the Fe/SiO₂-h.

The acidic properties of silica support and all activated catalysts were examined by NH₃-TPD, and the results are shown in Figure 4d. The desorption of NH₃ was observed in the temperature range from 50–800 °C; low, moderate, and high temperature correspond to the weak, medium and strong acid site on the surface [57]. Two distinct NH₃ desorption peaks were observed from the profile of silica support, indicating the presence of at least two different acid sites on the surface. A well-defined peak with high intensity at 115 °C is assigned to the desorption of NH₃ from a weak acid site, whereas a large broad peak centered at 410 °C is considered as the desorption from a strong acid site. When compared with the profile of all catalysts in the low temperature region, the support shows the highest of weak acidity, and tends to decrease due to the blocking effect of the iron particle in the

metal supported catalyst. Moreover, the profiles of all catalysts in the temperature range of 200–400 °C do not illustrate the NH₃ desorption peak. This could be explained by the medium acidity due to the support not being present for all activated catalysts (Fe/SiO₂-h, Fe/SiO₂-hc and Fe/SiO₂-c). However, the profile of activated catalysts with iron carbide (Fe/SiO₂-hc and Fe/SiO₂-c) remarkably depicts a broad peak above 400 °C. This could reflect the strong acid sites presenting on the surface of iron carbide. The desorption of the strong chemisorbed NH₃ on Fe/SiO₂-c shifts to a lower temperature. The strong Lewis acid sites on the carbide catalyst could be attributed to the vacancy sites exposed on the defects of the catalyst surface [58,59]. The following sequence of the activated catalysts relates to the amount of the strong acid sites: Fe/SiO₂-h (22.0 mmol/g) < Fe/SiO₂-hc (111.1 mmol/g) < Fe/SiO₂-c (357.1 mmol/g). Accordingly, the CO₂-TPD and NH₃-TPD results reveal that the carbonized catalyst (Fe/SiO₂-hc and Fe/SiO₂-c catalyst) provides a greater acidity, as well as basicity, compared to the reduced catalyst (Fe/SiO₂-h catalyst).

In summary of the results from all TPD techniques, the Fe/SiO₂-hc provides the highest H₂ adsorption capability. The Fe/SiO₂-c shows the greatest CO and CO₂ adsorption capability. The CO adsorption abilities of Fe/SiO₂-c and Fe/SiO₂-hc are much better than the Fe/SiO₂-h. The Fe/SiO₂-c and Fe/SiO₂-hc possessed a larger number of the strong Lewis acid sites. The existence of the acidic property on the surface plays an important role on the chemisorption of the intermediate CO occurring during RWGS, which is a reactant for the secondary reaction of hydrocarbon synthesis [60]. This information is further associated with results in the catalytic tests to explain the CO₂ hydrogenation performance of all activated catalysts.

2.4. Catalytic Performance of Materials

The effect of different iron phases obtained from the different method for activation of iron-based catalysts on the catalytic performance in CO₂ hydrogenation was examined under a mild reaction condition (temperature below 250 °C at the atmospheric pressure). To verify the role of the active phase of iron species in the reaction, the metallic iron (Fe/SiO₂-h), the iron carbide (Fe/SiO₂-c), and the combination of metallic iron and iron carbide (Fe/SiO₂-hc) are kept and remained in those forms during the mild reaction conditions. The catalytic performance of CO₂ hydrogenation performance is reported in Table 4 as the CO₂ conversions, the product selectivity, and the chain growth probabilities. Noticeably, the chain growth probabilities or alpha values were calculated from the slope of Anderson–Schulz Flory (ASF) plots in Figure 5.

Table 4. Catalytic performances of the catalysts with different activated conditions in the CO₂ hydrogenation reaction conditions ^a.

Catalysts (%)	CO ₂ Conv.	Alpha		Products Selectivity (%)		
		($\alpha_{C_6-C_{18}}$)	CO	C ₁	C ₂ –C ₄	C ₅₊
Fe/SiO ₂ -h	1.56	0.63	97.04	1.39	0.32	1.25
Fe/SiO ₂ -c	5.11	0.70	87.17	6.29	1.22	5.37
Fe/SiO ₂ -hc	4.52	0.68	87.08	6.95	2.23	3.74

^a Reaction conditions: T = 220 °C, p = 1 atm, CO₂/H₂ = 2/1, WHSV = 4920 mL/h.g.

The catalytic performance is reported in Table 4. The catalytic activity measured by the CO₂ conversion is rather low because of low operating conditions, which should not affect the change of the iron phase during the reaction. Among all activated catalysts, the Fe/SiO₂-c catalyst illustrates the highest CO₂ conversion (5.11%), with the highest selectivity toward C₅₊ (5.37%) product and the highest chain growth probability (7.00). The result of Fe/SiO₂-hc is very close to that of Fe/SiO₂-c. The Fe/SiO₂-hc establishes the CO₂ conversion of 4.52%, with the selectivity toward C₅₊ of 3.74% and the chain growth probability of 0.68. Differently, the Fe/SiO₂-h catalyst displays the lowest CO₂ conversion of 1.56% and the lowest selectivity toward C₅₊ of 1.25% with the chain growth probability

of 0.63. For CO selectivity, the Fe/SiO₂-h shows the highest CO selectivity (97.04%), while the Fe/SiO₂-c and the Fe/SiO₂-hc present a similar CO selectivity of about 87%.

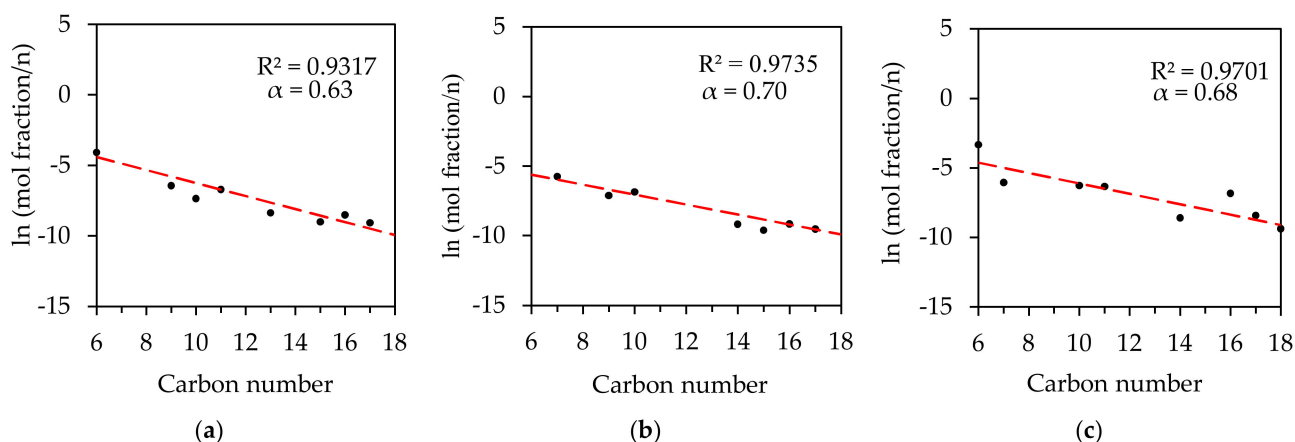


Figure 5. ASF plot and α values of (a) Fe/SiO₂-h, (b) Fe/SiO₂-c, and (c) Fe/SiO₂-hc catalysts. Reaction conditions: T = 220 °C, p = 1 atm, CO₂/H₂ = 2/1, WHSV = 4920 mL/h.g. (●) experiment, (—) model fitting.

To explain the results, the simplified pathway of the CO₂ hydrogenation process was drawn in Figure 6 using information from the literature involving three reactions: RWGS reaction, CO hydrogenation, and methanation reactions. The CO₂ molecules firstly react with H₂ to form CO and H₂O. The adsorbed CO molecules are hydrogenated into chemisorbed methylene (:CH₂) and then transformed into long-chain hydrocarbons [61]. In the case of full hydrogenation of the adsorbed CO, methane (CH₄) and by-product water can be produced via a methanation reaction [62]. This reaction pathway associated with reaction results and the TPD results implies that the CO₂ conversion and the hydrocarbon polymerization are promoted by the CO₂ adsorption, the CO adsorption, and the acidity of the catalyst surface. Therefore, a higher CO₂ conversion, as well as a better selectivity toward C₅₊, were found in the catalysts with iron carbide (Fe/SiO₂-c and Fe/SiO₂-hc) which have a greater CO₂ adsorption, CO adsorption, and acidity than the catalyst with only metallic iron (Fe/SiO₂-h). Such good chemisorption, textural, structural, and chemical properties lead to an effective polymerization. Because the Fe/SiO₂-h has the lowest CO adsorption capability, this catalyst possesses the highest CO selectivity. Between the Fe/SiO₂-c and the Fe/SiO₂-hc, the Fe/SiO₂-c provides a higher selectivity toward C₅₊, as the Fe/SiO₂-hc adsorbs more hydrogen on the surface resulting in the shorter hydrocarbon products.

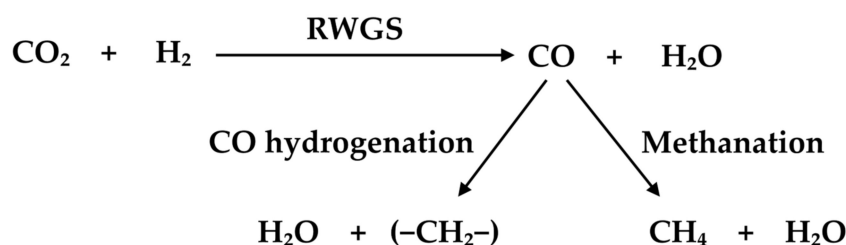


Figure 6. Illustration of the reaction pathway of CO₂ hydrogenation into hydrocarbon products.

3. Materials and Methods

3.1. Catalyst Preparation

High surface area silica material used as catalyst support was synthesized using the precipitation method. Briefly, a Pluronic P123 in a dilute hydrochloric solution was stirred until the solution was clear. After that, n-butanol solution was added at 35 °C and then

was stirred for 1 h. TEOS was then added to the solution and was continuously stirred for 24 h. Afterwards, it was transferred to an autoclave, sealed, and aged for 48 h. The precipitated white slurry was washed with distilled water until a pH of approximately 7. After completing the washing process, the colloidal suspension of SiO₂ was dried in the oven and calcined in flowing air at 550 °C for 2 h. The calcined SiO₂ was pressed into pellets and then crushed and sieved to obtain 355–710 µm of particle size. The Fe/SiO₂ catalyst was prepared by an incipient wetness impregnation method using iron nitrate solution as a precursor. The solution was added dropwise into the SiO₂ support. The impregnated catalyst was settled and aged overnight. Then, it was dried and calcined at 550 °C for 2 h to give Fe/SiO₂ catalyst at metal loading of 20%wt. Element analysis of 20%wt Fe/SiO₂ catalyst using AAS gives the Fe content of 18.59%wt.

The activation of Fe/SiO₂ was performed by three different activation procedures before the reaction process. These procedures are given as below:

Procedure 1: the calcined Fe/SiO₂ catalyst was reduced in pure H₂ at 500 °C for 16 h with a heating rate of 2 °C/min. The catalyst was denoted as Fe/SiO₂-h.

Procedure 2: the calcined Fe/SiO₂ catalyst was only carbonized in a flow of 10% CO/He at 400 °C for 2 h with a heating rate of 2 °C/min. This catalyst was denoted as Fe/SiO₂-c.

Procedure 3: the calcined Fe/SiO₂ catalyst was firstly reduced in pure H₂ at 500 °C for 16 h with a heating rate of 2 °C/min. Subsequently, the reduced Fe/SiO₂ was carbonized in a flow of 10% CO/He at 400 °C with a heating rate of 2 °C/min for 2 h. This catalyst was denoted as Fe/SiO₂-hc.

3.2. Catalyst Characterizations

3.2.1. N₂ Adsorption-Desorption

N₂ adsorption–desorption analysis was performed at –196 °C (liquid N₂ temperature) in BELSORP-mini with BELPREP-flow (BEL, BEL Japan, Inc., Osaka, Japan) apparatus, using a volumetric gas adsorption method. Prior to the experiment, the catalyst surfaces were outgassed at 350 °C under He atmosphere overnight. N₂ adsorption–desorption isotherm was measured in the range of relative pressure (p/p_0) from 10^{–4} to 1.0. The specific total surface area (S_{BET}), average pore diameter (D_p), and total pore volume (V_{tp}) were calculated by the BET (Brunauer-Emmett-Teller) method. Micropore volume ($V_{\mu\text{p}}$) was analyzed by t -plot method. Pore size distributions of mesopore and micropore were calculated by the BJH (Barrett, Joyner and Halenda) and MP (Micropore analysis) methods, respectively.

3.2.2. Temperature-Programmed Reduction (TPR)

The reduction behavior of the calcined Fe/SiO₂ catalyst was studied by hydrogen temperature-programmed reduction (H₂-TPR). The H₂-TPR was carried out on a BELCAT-B (BEL, BEL Japan, Inc.) equipped with a thermal conductivity detector (TCD). Prior to the measurement, the catalyst sample was cleaned under Ar atmosphere at 200 °C for 50 min. Subsequently, the catalyst was exposed in a flow of 5% H₂/Ar (30 mL/min) from ambient temperature to 800 °C with a heating rate of 10 °C/min. Water produced from the reduction was removed and trapped by molecular sieve (zeolite). H₂ consumption during the reduction process was detected by TCD and displayed as H₂-TPR profile.

Temperature-programmed reduction of carbon monoxide (CO-TPR) was used to determine the carbonization behavior of the calcined Fe/SiO₂ catalyst and reduced Fe/SiO₂ catalyst. CO-TPR profiles were carried out on the BELCAT-B equipment (BEL, BEL Japan, Inc.) with TCD. The procedure of CO-TPR of the calcined Fe/SiO₂ catalyst and reduced Fe/SiO₂ catalyst was performed in the same manner as H₂-TPR, but using 10% CO/He instead. CO₂ produced from the carbonization reaction was trapped by molecular sieve 5A (calcium aluminosilicate, purified), while CO consumed was simultaneously detected by TCD and presented as CO-TPR profile.

3.2.3. X-ray Diffraction (XRD)

Powder XRD patterns of calcined Fe/SiO₂ and activated catalysts (Fe/SiO₂-h, Fe/SiO₂-hc, and Fe/SiO₂-c) were obtained on a Bruker D8 diffractometer equipped with a Cu K α source ($\lambda = 1.54056$ angstrom). The operating voltage and current were 40 kV and 40 mA in the range of 2θ from 20° to 80°, with a step size of 0.02°. The XRD patterns of catalysts were collected at 1 s per step. The average crystallite size was calculated based on the broadening of X-ray diffraction lines using the Scherrer formula.

3.2.4. Raman Spectroscopy

Raman spectra were acquired by using a FT-Raman spectrometer system (Perkin Elmer spectrum GX) equipped with a laser excitation with a wavelength of 532 nm. The Raman signal was monitored in the Raman shift range of 100–3500 cm⁻¹ and the spectrum acquisition time was 100 s.

3.2.5. Temperature-Programmed Desorption (TPD)

The adsorption-desorption properties of activated catalysts were conducted using a BELCAT-B (BEL, BEL Japan, Inc.) equipped with TCD. Prior to the TPD measurement, all catalysts were activated in situ with three different condition methods, as mentioned above. The temperature-programmed desorption peak was integrated and compared to pulse calibration in order to calculate the gas adsorbed amount on the surface.

For H₂-TPD, the activated catalyst was exposed to H₂ flow at 120 °C for 30 min, followed by cooling down to ambient temperature and kept under Ar flow for 20 min to remove the weakly adsorbed H₂ species. The measurement was carried out from ambient temperature to 800 °C with a heating rate of 10 °C/min under the same inert gas.

For CO₂-TPD (or CO-TPD), the activated catalyst was saturated in a flow of pure CO₂ (or 10% CO/He) at 40 °C for 30 min. The catalyst was then switched to pure He for 20 min. The TPD measurement was undertaken from ambient temperature to 800 °C with a heating rate of 10 °C/min under the same inert gas.

For NH₃-TPD, the activated catalysts were saturated by means of the NH₃ adsorption. Prior to measurement, the catalyst surface was exposed to 5% NH₃/He at 50 °C for 30 min, followed by flushing in He. The TPD was performed in the same procedure with other TPD techniques.

3.3. Catalytic Activity Test

A CO₂ hydrogenation reaction over different activated catalysts was conducted in a stainless steel fixed-bed reactor under steady-state conditions. Firstly, the catalyst of 1.0 g was reduced in situ with different activation conditions. After the pretreatment, the catalyst surface was suddenly cooled down and maintained at 220 °C under a He flow at ambient pressure. Afterwards, the reaction mixture of CO₂, H₂, and N₂ (CO₂:H₂:N₂ = 50:25:7 mL/min) was fed into a reactor at 220 °C, 1 atm and 4920 mL/h.g of WHSV for 48 h. During the reaction, the gaseous phase products were analyzed by an on-line gas chromatograph (GC) (Model 450-GC, Bruker) equipped with a flame ionization detector and thermal conductivity detector. The liquid phase products were analyzed by an off-line GC (Model 430, Bruker) using a flame ionization detector. CO₂ conversion, CO selectivity, hydrocarbons selectivity, and the chain growth probability (Alpha; α) were calculated according to Equations (8)–(11), respectively [63].

$$\text{CO}_2 \text{ conversion (\%)} = [(\text{CO}_2 \text{ in} - \text{CO}_2 \text{ out}) / \text{CO}_2 \text{ in}] \times 100 \quad (8)$$

when CO₂ *in*: mole fraction of CO₂ in the inlet, whereas CO₂ *out*: mole fraction of CO₂ in the outlet.

$$\text{CO selectivity (\%)} = \left[\text{CO out} / \sum_{i=1}^n \text{Mole of } C_i \text{ hydrocarbons} \right] \times 100 \quad (9)$$

$$C_i \text{ hydrocarbon selectivity (\%)} = \left[\text{Mole of } C_i \text{ hydrocarbons} / \sum_{i=1}^n \text{Mole of } C_i \text{ hydrocarbons} \right] \times 100 \quad (10)$$

$$M_n/n = (1-\alpha)^2 \times \alpha^{n-1} \quad (11)$$

when M_n/n : the mole fraction of a hydrocarbon with carbon number (n), whereas α : the chain growth probability.

4. Conclusions

In this study, three activation conditions were used to prepare different iron phases on activated Fe/SiO₂ catalysts: the one-step H₂ reduction, the one-step CO carbonization, and the two-step H₂ reduction followed by CO carbonization. The analysis of the XRD and Raman spectrum demonstrates that the metallic iron phase was formed by the reduction under H₂ atmosphere (Fe/SiO₂-h) and the iron carbide phase was obtained by the carbonization under CO atmosphere (Fe/SiO₂-c). The iron carbide and the metallic iron combination were received from the two-step activation, the initial reduction under H₂ atmosphere followed by the carbonization under CO atmosphere (Fe/SiO₂-hc). The results from all TPD techniques and the CO₂ hydrogenation reaction in the mild conditions indicate that the lowest CO₂ conversion with the highest selectivity toward CO was observed on the Fe/SiO₂-h, as it possesses the lower CO₂ and CO adsorption capabilities. The activated catalysts with iron carbide (Fe/SiO₂-c and Fe/SiO₂-hc) provide the higher performance in terms of CO₂ conversion and the selectivity toward hydrocarbon products compared to the activated catalysts with metallic iron (Fe/SiO₂-h), due to the greater CO₂ and CO adsorption capabilities. Moreover, the surface of iron carbide species has more defects compared to the reduced catalyst, leading to the increase of adsorbed CO occurring during RWGS. The defects of the catalyst surface promote the weakening of the C–O bond of CO₂ resulting in the increase of adsorbed CO existing on the active site. The higher selectivity towards light hydrocarbon products (C₁ and C₂–C₄) is obtained with Fe/SiO₂-hc, whereas the high selectivity to C₅₊ hydrocarbons is gained from Fe/SiO₂-c. This is because Fe/SiO₂-hc has a better H₂ adsorption capability, while Fe/SiO₂-c acquires a greater acidity on the surface. This work provides detailed investigations of the chemisorption, textural, structural, and chemical properties in relation to CO₂ hydrogenation over different phases of iron-based catalyst, giving potential to offer guidance for the proper design of highly efficient catalysts in CO₂ hydrogenation.

Author Contributions: Conceptualization, P.S. and S.T.; methodology, P.S., M.P., T.R. and S.T.; formal analysis, P.S., M.P., T.R. and S.T.; investigation, P.S., M.P., T.R. and S.T.; resources, P.S., M.P., T.S., T.R. and S.T.; data curation, P.S., M.P., T.R. and S.T.; writing—original draft preparation, P.S., M.P., T.R. and S.T.; writing—review and editing, P.S., M.P., T.R. and S.T.; visualization, P.S. and S.T.; supervision, M.P. and S.T.; project administration, S.T.; funding acquisition, T.S. and S.T. All authors have read and agreed to the published version of the manuscript.

Funding: This research was funded by the National Research Council of Thailand (NRCT) via Research and Researchers for Industries (RRI) and PTT Public Company Limited, Thailand, grant number PHD59I0082.

Data Availability Statement: Not applicable.

Acknowledgments: The authors would like to thank the National Research Council of Thailand (NRCT) via the Research and Researchers for Industries (RRI) and PTT Public Company Limited, Thailand, grant number PHD59I0082, for the supporting financial fund. Moreover, we would like to acknowledge Eric Croiset, Chemical Engineering, University of Waterloo, Canada, for the support of partially analytical apparatus.

Conflicts of Interest: The authors declare no conflict of interest.

References

1. Metz, B.; Davidson, O.; De Coninck, H.C.; Loos, M.; Meyer, L. *IPCC Special Report on Carbon Dioxide Capture and Storage*, 1st ed.; Cambridge University Press: Cambridge, UK, 2005; p. 442.
2. Li, Q.; Huang, T.; Zhang, Z.; Xiao, M.; Gai, H.; Zhou, Y.; Song, H. Highly Efficient Hydrogenation of CO₂ to Formic Acid over Palladium Supported on Dication Poly(ionic liquid)s. *Mol. Catal.* **2021**, *509*, 111644. [[CrossRef](#)]
3. Xu, D.; Hong, X.; Liu, G. Highly dispersed metal doping to ZnZr oxide catalyst for CO₂ hydrogenation to methanol: Insight into hydrogen spillover. *J. Catal.* **2021**, *393*, 207–214. [[CrossRef](#)]
4. Zhou, W.; Cheng, K.; Kang, J.; Zhou, C.; Subramanian, V.; Zhang, Q.; Wanf, Y. New horizon in C1 chemistry: Breaking the selectivity limitation in transformation of syngas and hydrogenation of CO₂ into hydrocarbon chemicals and fuels. *Chem. Soc. Rev.* **2019**, *48*, 3193–3228. [[CrossRef](#)]
5. Liu, R.; Ma, Z.; Sears, J.D.; Juneau, M.; Neidig, M.L.; Porosoff, M.D. Identifying correlations in Fischer-Tropsch synthesis and CO₂ hydrogenation over Fe-based ZSM-5 catalysts. *J. CO₂ Util.* **2020**, *41*, 101290. [[CrossRef](#)]
6. Han, S.J.; Hwang, S.M.; Park, H.G.; Zhang, C.; Jun, K.W.; Kim, S.K. Identification of active sites for CO₂ hydrogenation in Fe catalysts by first-principles microkinetic modelling. *J. Mater. Chem. A* **2020**, *8*, 13014–13023. [[CrossRef](#)]
7. Zhang, S.; Liu, X.; Shao, Z.; Wang, H.; Sun, Y. Direct CO₂ hydrogenation to ethanol over supported Co₂C catalysts: Studies on support effects and mechanism. *J. Catal.* **2020**, *382*, 86–96. [[CrossRef](#)]
8. You, Z.; Deng, W.; Zhang, Q.; Wang, Y. Hydrogenation of carbon dioxide to light olefins over non-supported iron catalyst. *Chin. J. Catal.* **2013**, *34*, 956–963. [[CrossRef](#)]
9. Yuan, F.; Zhang, G.; Zhu, J.; Ding, F.; Zhang, A.; Song, C.; Guo, X. Boosting light olefin selectivity in CO₂ hydrogenation by adding Co to Fe catalysts within close proximity. *Catal. Today* **2021**, *371*, 142–149. [[CrossRef](#)]
10. Dry, M.E.; Hoogendoorn, J.C. Technology of the Fischer-Tropsch Process. *Catal. Rev.* **1981**, *23*, 265–278. [[CrossRef](#)]
11. Li, J.; Smith, K.J. Methane decomposition and catalyst regeneration in a cyclic mode over supported Co and Ni catalysts. *Appl. Catal. A Gen.* **2008**, *349*, 116–124. [[CrossRef](#)]
12. Röper, M. Fischer-Tropsch Synthesis. In *Catalysis in C1 Chemistry. Catalysis by Metal Complexes*; Keim, W., Ed.; Springer: Dordrecht, The Netherlands, 1983; pp. 41–88.
13. Ramirez, A.; Giver's, L.; Bavykina, A.; Ould-Chikh, S.; Gascon, J. Metal Organic Framework-Derived Iron Catalysts for the Direct Hydrogenation of CO₂ to Short Chain Olefins. *ACS Catal.* **2018**, *8*, 9174–9182. [[CrossRef](#)]
14. Jager, B.; Dry, M.E.; Shingles, T.; Steynberg, A.P. Experience with a new type of reactor for fischer-tropsch synthesis. *Catal. Lett.* **1990**, *7*, 293–301. [[CrossRef](#)]
15. Liu, J.X.; Wang, P.; Xu, W.; Hensen, E.J.M. Particle Size and Crystal Phase Effects in Fischer-Tropsch Catalysts. *Engineering* **2017**, *3*, 467–476. [[CrossRef](#)]
16. Gnanamani, M.K.; Jacobs, G.; Hamdeh, H.H.; Shafer, W.D.; Liu, F.; Hopps, S.D.; Thomas, G.A.; Davis, B.H. Hydrogenation of Carbon Dioxide over Co-Fe Bimetallic Catalysts. *ACS Catal.* **2016**, *6*, 913–927. [[CrossRef](#)]
17. Chou, C.Y.; Loiland, J.A.; Lobo, R.F. Reverse water-gas shift iron catalyst derived from magnetite. *Catalysts* **2019**, *9*, 773. [[CrossRef](#)]
18. Pastor-Pérez, L.; Baibars, F.; Le Sache, E.; Arellano-García, H.; Gu, S.; Reina, T.R. CO₂ valorisation via Reverse Water-Gas Shift reaction using advanced Cs doped Fe-Cu/Al₂O₃ catalysts. *J. CO₂ Util.* **2017**, *21*, 423–428. [[CrossRef](#)]
19. Luo, M.; Hamdeh, H.; Davis, B.H. Fischer-Tropsch Synthesis. Catalyst activation of low alpha iron catalyst. *Catal. Today* **2009**, *140*, 127–134. [[CrossRef](#)]
20. Abelló, S.; Montané, D. Exploring iron-based multifunctional catalysts for fischer-tropsch synthesis: A review. *ChemSusChem* **2011**, *4*, 1538–1556. [[CrossRef](#)]
21. Sudsakorn, K.; Goodwin, J.G.; Adeyiga, A.A. Effect of activation method on Fe FTS catalysts: Investigation at the site level using SSITKA. *J. Catal.* **2003**, *213*, 204–210. [[CrossRef](#)]
22. Pijolat, M.; Perrichon, V.; Bussière, P. Study of the carburization of an iron catalyst during the Fischer-Tropsch synthesis: Influence on its catalytic activity. *J. Catal.* **1987**, *107*, 82–91. [[CrossRef](#)]
23. Otun, K.O.; Yao, Y.; Liu, X.; Hildebrandt, D. Synthesis, structure, and performance of carbide phases in Fischer-Tropsch synthesis: A critical review. *Fuel* **2021**, *296*, 120689. [[CrossRef](#)]
24. Lu, F.; Chen, X.; Lei, Z.; Wen, L.; Zhang, Y. Revealing the activity of different iron carbides for Fischer-Tropsch synthesis. *Appl. Catal. B Environ.* **2021**, *281*, 119521. [[CrossRef](#)]
25. Zhu, J.; Zhang, G.; Li, W.; Zhang, X.; Ding, F.; Song, C.; Guo, X. Deconvolution of the Particle Size Effect on CO₂ Hydrogenation over Iron-Based Catalysts. *ACS Catal.* **2020**, *10*, 7424–7433. [[CrossRef](#)]
26. Liu, J.; Zhang, G.; Jiang, X.; Wang, J.; Song, C.; Guo, X. Insight into the role of Fe₅C₂ in CO₂ catalytic hydrogenation to hydrocarbons. *Catal. Today* **2020**, *371*, 162–170. [[CrossRef](#)]
27. Jozwiak, W.K.; Kaczmarek, E.; Maniecki, T.P.; Ignaczak, W.; Maniukiewicz, W. Reduction behavior of iron oxides in hydrogen and carbon monoxide atmospheres. *Appl. Catal. A Gen.* **2007**, *326*, 17–27. [[CrossRef](#)]
28. Utsis, N.; Vidruk-Nehemya, R.; Landau, M.V.; Herskowitz, M. Novel bifunctional catalysts based on crystalline multi-oxide matrices containing iron ions for CO₂ hydrogenation to liquid fuels and chemicals. *Faraday Discuss* **2016**, *188*, 545–563. [[CrossRef](#)]
29. Dai, C.; Zhao, X.; Hu, B.; Zhang, J.; Hao, Q.; Chen, H.; Guo, X.; Ma, X. Hydrogenation of CO₂ to Aromatics over Fe-K/Alkaline Al₂O₃ and P/ZSM-5 Tandem Catalysts. *Ind. Eng. Chem. Res.* **2020**, *59*, 19194–19202. [[CrossRef](#)]

30. Jin, Y.; Datye, A.K. Phase transformations in iron Fischer-Tropsch catalysts during temperature-programmed reduction. *J. Catal.* **2000**, *196*, 8–17. [[CrossRef](#)]
31. Mai, K. Effects of Different Preparation Methods on Structure and Catalytic Behavior of Iron-Based Catalyst via Fischer Tropsch Synthesis of Biomass-Derived Syngas. Master's Thesis, Louisiana State University and Agricultural and Mechanical College, Baton Rouge, LA, USA, 2014.
32. Kirchner, J.; Anolleck, J.K.; Lösch, H.; Kureti, S. Methanation of CO₂ on iron based catalysts. *Appl. Catal. B Environ.* **2018**, *223*, 47–59. [[CrossRef](#)]
33. Tahari, M.N.A.; Salleh, F.; Saharuddin, T.S.T.; Dzakaria, N.; Samsuri, A.; Hisham, M.W.M.; Yarmo, M.A. Influence of hydrogen and various carbon monoxide concentrations on reduction behavior of iron oxide at low temperature. *Int. J. Hydrog. Energy* **2019**, *44*, 20751–20759. [[CrossRef](#)]
34. Niu, L.; Liu, X.; Wen, X.; Yang, Y.; Xu, J.; Li, Y. Effect of potassium promoter on phase transformation during H₂ pretreatment of a Fe₂O₃ Fischer Tropsch synthesis catalyst precursor. *Catal. Today* **2020**, *343*, 101–111. [[CrossRef](#)]
35. Pendyala, V.R.R.; Jacobs, G.; Mohandas, J.C.; Luo, M.; Ma, W.; Gnanamani, M.K.; Davis, B.H. Fischer-Tropsch synthesis: Attempt to tune FTS and WGS by alkali promoting of iron catalysts. *Appl. Catal. A Gen.* **2010**, *389*, 131–139. [[CrossRef](#)]
36. Chai, J.; Pestman, R.; Chen, W.; Dugulan, A.I.; Feng, B.; Men, Z.; Wang, P.; Hensen, E.J.M. The role of H₂ in Fe carburization by CO in Fischer-Tropsch catalysts. *J. Catal.* **2021**, *400*, 93–102. [[CrossRef](#)]
37. Bian, G.; Oonuki, A.; Koizumi, N.; Nomoto, H.; Yamada, M. Studies with a precipitated iron Fischer-Tropsch catalyst reduced by H₂ or CO. *J. Mol. Catal. A Chem.* **2002**, *186*, 203–213. [[CrossRef](#)]
38. Alayat, A.; McIlroy, D.N.; McDonald, A.G. Effect of synthesis and activation methods on the catalytic properties of silica nanospring (NS)-supported iron catalyst for Fischer-Tropsch synthesis. *Fuel Process. Technol.* **2018**, *169*, 132–141. [[CrossRef](#)]
39. Tahari, M.N.A.; Salleh, F.; Saharuddin, T.S.T.; Samsuri, A.; Samidin, S.; Yarmo, M.A. Influence of hydrogen and carbon monoxide on reduction behavior of iron oxide at high temperature: Effect on reduction gas concentrations. *Int. J. Hydrog. Energy* **2021**, *46*, 24791–24805. [[CrossRef](#)]
40. Nielsen, M.R.; Moss, A.B.; Bjørnlund, A.S.; Liu, X.; Knop-Gericke, A.; Klyushin, A.Y.; Grunwaldt, J.D.; Sheppard, T.L.; Doronkin, D.E.; Zimina, A.; et al. Reduction and carburization of iron oxides for Fischer-Tropsch synthesis. *J. Energy Chem.* **2020**, *51*, 48–61. [[CrossRef](#)]
41. Ni, Z.; Kang, S.; Bai, J.; Li, Y.; Huang, Y.; Wang, Z.; Qin, H.; Li, X. Uniformity dispersive, anti-coking core@double-shell-structured Co@SiO₂@C: Effect of graphitic carbon modified interior pore-walls on C₅₊ selectivity in Fischer-Tropsch synthesis. *J. Colloid Interface Sci.* **2017**, *505*, 325–331. [[CrossRef](#)]
42. Zhang, Y.; Cao, C.; Zhang, C.; Zhang, Z.; Liu, X.; Yang, Z.; Zhu, M.; Meng, B.; Xu, J.; Han, Y.F. The study of structure-performance relationship of iron catalyst during a full life cycle for CO₂ hydrogenation. *J. Catal.* **2019**, *378*, 51–62. [[CrossRef](#)]
43. Guo, T.Y.; Liu, S.Y.; Qing, M.; Feng, J.L.; Lü, Z.G.; Wang, H.; Yang, Y. In situ XRD study of the effect of H₂O on Fe₅C₂ phase and Fischer-Tropsch performance. *J. Fuel Chem. Technol.* **2020**, *48*, 75–82. [[CrossRef](#)]
44. Ding, M.; Yang, Y.; Wu, B.; Li, Y.; Wang, T.; Ma, L. Study on reduction and carburization behaviors of iron-based Fischer-Tropsch synthesis catalyst. *Energy Procedia* **2014**, *61*, 2267–2270. [[CrossRef](#)]
45. Jedrzejewska, A.; Costa, S.; Cendrowski, K.; Kalenczuk, R.J.; Mijowska, E. Synthesis and characterization of iron-filled multi-walled nanotubes. *Mater. Sci. Pol.* **2011**, *29*, 299–304. [[CrossRef](#)]
46. Ding, M.; Yanga, Y.; Wu, B.; Xua, J.; Zhang, C.; Xiang, H.; Li, Y. Study of phase transformation and catalytic performance on precipitated iron-based catalyst for Fischer-Tropsch synthesis. *J. Mol. Catal. A Chem.* **2009**, *303*, 65–71. [[CrossRef](#)]
47. Kryszak, D.; Stawicka, K.; Trejda, M. Calcium and nitrogen species loaded into SBA-15-a promising catalyst tested in Knoevenagel condensation. *Dalt. Trans.* **2020**, *49*, 9781–9794. [[CrossRef](#)] [[PubMed](#)]
48. Niu, H.; Lu, J.; Song, J.; Pan, L.; Zhang, X.; Wang, L.; Zou, J.J. Iron Oxide as a Catalyst for Nitroarene Hydrogenation: Important Role of Oxygen Vacancies. *Ind. Eng. Chem. Res.* **2016**, *55*, 8527–8533. [[CrossRef](#)]
49. Bozso, F.; Ertl, G.; Grunze, M.; Weiss, M. Chemisorption of hydrogen on iron surfaces. *Appl. Surf. Sci.* **1977**, *1*, 103–119. [[CrossRef](#)]
50. Zhang, C.; Zhao, G.; Liu, K.; Yang, Y.; Xiang, H.; Li, Y. Adsorption and reaction of CO and hydrogen on iron-based Fischer-Tropsch synthesis catalysts. *J. Mol. Catal. A Chem.* **2010**, *328*, 35–43. [[CrossRef](#)]
51. Gao, F.; Wang, H.; Qing, M.; Yang, Y.; Li, Y. Controlling the phase transformations and performance of iron-based catalysts in the Fischer-Tropsch synthesis. *Chin. J. Catal.* **2013**, *34*, 1312–1325. [[CrossRef](#)]
52. Ratnasamy, C.; Wagner, J. Water gas shift catalysis. *Catal. Rev.* **2009**, *51*, 325–440. [[CrossRef](#)]
53. Zou, C.; Duin, V.A.C.T.; Sorescu, D.C. Theoretical investigation of hydrogen adsorption and dissociation on iron and iron carbide surfaces using the ReaxFF reactive force field method. *Top Catal.* **2012**, *55*, 391–401. [[CrossRef](#)]
54. Centi, G.; Perathoner, S. Opportunities and prospects in the chemical recycling of carbon dioxide to fuels. *Catal. Today* **2009**, *148*, 191–205. [[CrossRef](#)]
55. Gaube, J.; Klein, H.F. Studies on the reaction mechanism of the Fischer-Tropsch synthesis on iron and cobalt. *J. Mol. Catal. A Chem.* **2008**, *283*, 60–68. [[CrossRef](#)]
56. Lyu, S.; Wang, L.; Li, Z.; Yin, S.; Chen, J.; Zhang, Y.; Li, J.; Wang, Y. Stabilization of ε-iron carbide as high-temperature catalyst under realistic Fischer-Tropsch synthesis conditions. *Nat. Commun.* **2020**, *11*, 6219. [[CrossRef](#)]
57. Hu, Z.P.; Chen, L.; Chen, C.; Yuan, Z.Y. Fe/ZSM-5 catalysts for ammonia decomposition to CO_x-free hydrogen: Effect of SiO₂/Al₂O₃ ratio. *Mol. Catal.* **2018**, *455*, 14–22. [[CrossRef](#)]

58. Cao, D.B.; Li, Y.W.; Wang, J.; Jiao, H. Chain growth mechanism of Fischer-Tropsch synthesis on $\text{Fe}_5\text{C}_2(0\ 0\ 1)$. *J. Mol. Catal. A Chem.* **2011**, *346*, 55–69. [[CrossRef](#)]
59. Ozbek, M.O.; Niemantsverdriet, J.W. Elementary reactions of CO and H_2 on C-terminated $\chi\text{-Fe}_5\text{C}_2(0\ 0\ 1)$ surfaces. *J. Catal.* **2014**, *317*, 158–166. [[CrossRef](#)]
60. Wang, X.; Wu, D.; Zhang, J.; Gao, X.; Ma, Q.; Fan, S.; Zhao, T.S. Highly selective conversion of CO_2 to light olefins via Fischer-Tropsch synthesis over stable layered K-Fe-Ti catalysts. *Appl. Catal. A Gen.* **2019**, *573*, 32–40. [[CrossRef](#)]
61. Boreriboon, N.; Jiang, X.; Song, C.; Prasassarakich, P. Fe-based bimetallic catalysts supported on TiO_2 for selective CO_2 hydrogenation to hydrocarbons. *J. CO₂ Util.* **2018**, *25*, 330–337. [[CrossRef](#)]
62. Merkache, R.; Fechete, I.; Maamache, M.; Bernard, M.; Turek, P.; Al-Dalama, K.; Garin, F. 3D ordered mesoporous Fe-KIT-6 catalysts for methylcyclopentane (MCP) conversion and carbon dioxide (CO_2) hydrogenation for energy and environmental applications. *Appl. Catal. A Gen.* **2015**, *504*, 672–681. [[CrossRef](#)]
63. Mierczynski, P.; Dawid, B.; Chalupka, K.; Maniukiewicz, W.; Witonska, I.; Szyrkowska, M.I. Role of the activation process on catalytic properties of iron supported catalyst in Fischer-Tropsch synthesis. *J. Energy Inst.* **2020**, *93*, 565–580. [[CrossRef](#)]